MULTI-MODAL EXTREME-ULTRAVIOLET REFLECTOMETER: SOLVING INVERSE PROBLEMS IN NANOSTRUCTURE METROLOGY

Yunzhe Shao[1], Nicholas W. Jenkins[1], Clay Klein[1], Yunhao Li[1], Yuka Esashi[1], Margaret M. Murnane[1], Henry C. Kapteyn[1,2], Michael Tanksalvala[1,3]

[1]Department of Physics, JILA, and STROBE NSF Science and Technology Center, University of Colorado Boulder and NIST, Boulder, CO 80309, USA
[2]KMLabs Inc., Boulder, CO 80301, USA
[3]Applied Physics Division, National Institute of Standards and Technology, Boulder, CO 80305, USA

ABSTRACT

Coherent extreme-ultraviolet (EUV) light offers researchers chemical specificity and spatial resolution that is ideal for nanostructure metrology. Combining appropriate physical forward models that capture EUV light-sample interactions and propagation, the experimental data, and optimization routines, one can measure important parameters of nanostructured samples. In this paper, we discuss a unique instrument, designed to characterize the multilayer composition, geometry, topography, and interface quality of various nanostructured samples. We utilize the advantage of coherent EUV light and demonstrate three modes of characterizations, including reflectometry, scatterometry, and coherent diffractive imaging (CDI) reflectometry.

Index Terms— Inverse problem, extreme-ultraviolet light, reflectometry, scatterometry, coherent diffractive imaging

1. INTRODUCTION

Modern semiconductors as well as quantum devices can benefit tremendously from characterization techniques that have nanoscale resolution, are non-destructive, and comprehensive enough to capture the relevant parameters of a sample [1,2]. As devices scale in size and incorporate 3D structures, the tolerance for imperfections in interfaces and multilayer fabrications become progressively more stringent. Standard characterization techniques within the industry include scanning electron microscopy (SEM), optical and x-ray reflectometry and scatterometry, ellipsometry, atomic force microscopy (AFM), and scanning transmission electron microscopy (STEM). These techniques are sensitive to different device parameters, and often must be combined and conducted in parallel since no single metrology technique can capture all the important parameters. In this paper, we explore a unique characterization technique by combining reflectometry, scatterometry, and coherent diffractive imaging (CDI) reflectometry in a different range of wavelengths [3-5].

Coherent, extreme-ultraviolet (EUV) light has exceptional capabilities for characterizing the composition and structure of nanomaterials, achieve far higher resolution and contrast than is possible using visible light. The distinct response of different elements upon illumination with EUV light leads to elemental specificity (i.e. amplitude and phase contrast) [6]. And the use of shorter wavelength, in combination with coherent diffractive imaging (CDI), where the spatial resolution is only limited by the numerical aperture (NA).

Here we present a tabletop EUV imaging reflectometer for high-fidelity metrology of nanostructures. The reflectometer is capable of three measurement modes: intensity reflectometry, scatterometry, and coherent diffractive imaging reflectometry. In each mode, the reflected EUV light is collected on a CCD camera. To analyze the reflected signal, an appropriate forward model of the EUV light-sample interaction and propagation is utilized and combined with an optimization of the model parameters to fit to the experimental reflection data. By solving the inverse problem of sampler determination from the collected EUV reflection, we are able to determine sample parameters with elemental specificity and high spatial resolution. The samples chosen for measurement and analysis highlight the applicability of EUV metrology to a wide range of semiconductor and material science systems [3,4].

2. EXPERIMENTAL SETUP: REFLECTOMETER

Figure 1(a) shows a simplified schematic of the experimental setup of the tabletop EUV reflectometer. A modelocked Ti:sapphire laser of 795 nm center wavelength, 80MHz repetition rate, and 5 nJ pulse energy seeds a Ti:sapphire regenerative amplifier (KMLabs Wyvern HP), which then outputs a pulse train of 795 nm center wavelength, 38 fs pulse duration, 3kHz repetition rate, and up to 2.6 mJ pulse energy.
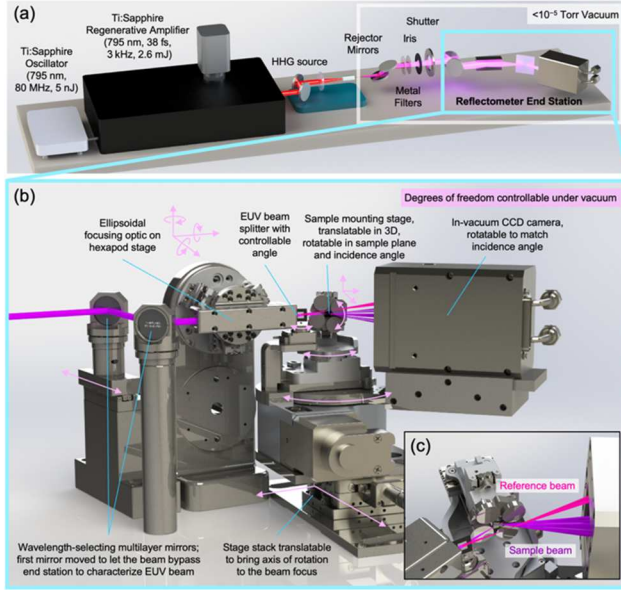
Figure 1. Multi-modal extreme ultraviolet tabletop reflectometer setup. (a) Schematic of the entire beam line. (b) Schematic of the reflectometer end station. Degrees of freedom that are controllable under vacuum are indicated by pink arrows. (c) Zoom-in of the end station from a different angle, showing that the reflected beam from the beam splitter ("reference beam") is directed straight to the camera to act as a reference beam; the transmitted beam reflects off the sample ("sample beam"). Figure adapted from [3].

The ultrafast laser pulse is focused into either a hollow-core waveguide or a semi-infinite gas cell to generate high brightness at photon energies spanning 30-100 eV depending on various source and generation parameters.

The rest of the beam line is kept at vacuum of 10^{-5} Torr or better to prevent absorption of the EUV light in air. After two rejector mirrors set at the Brewster angle of the IR driving laser and two adjustable filter enclosures, the EUV light enters the experiment end station, which is shown in Figure 1(b).

Inside the end station, the EUV light is further selected by a pair of 45° angle-of-incidence multilayer mirrors and into the custom ellipsoidal optic, focusing onto the sample with a demagnification of 22 times and a spot size of ~3 μm. The sample is mounted on a customized stack of stages that allow for 3D linear translation and sample in-plane rotation for navigation, orientation, and scanning, as well as a rotation around the vertical axis (viewed from the perspective of Figure 1(b)) to change the angle of incidence of the EUV light onto the sample.

The light is then collected by the in-vacuum CCD EUV camera, which is mounted on a rotation stage that rotates with the sample angle-of-incidence in a θ-2θ configuration, maintaining the reflected/diffracted EUV light on the camera as the angle-of-incidence is changed.
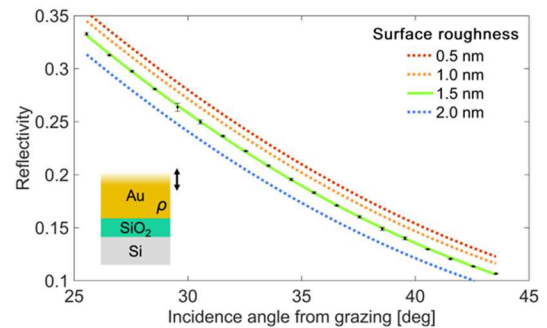
3. INTENSITY REFLECTOMETRY

The first mode of characterization we explore is intensity reflectometry, where we measure the specular reflectivity of the EUV beam illuminating a transversely uniform sample as a function of the incidence angle. Here, the goal is to characterize layer thicknesses, surface and interface roughnesses, and other material parameters such as mass density, etc.

For intensity reflectometry measurements, we insert a 50 nm thick Si membrane coated with 3 nm of Pt on a rotation stage between the focusing ellipsoidal optic and the sample stage stack, as shown in Figure 1(c). The coated membrane serves as a beam splitter that diverts part of the incident beam away from the sample and onto a corner of the CCD camera directly. This greatly improves the stability of reflectivity as we have a reference beam for normalization. As discussed in previous published work, we can achieve RMS stability that is very close to the shot noise limit in this configuration [3].

In this inverse problem, the physical forward model of light-sample interaction can be effectively generated using the Parratt formalism. The light-matter interaction of EUV photons is dominated by the core-shell electrons. Hence, the index of refraction n depends only on the number density of each elemental species and can be calculated using pre-characterized elemental scattering factors [6]:

$$n = 1 - \delta - i\beta = 1 - \frac{r_e}{2\pi}\lambda^2 \sum_j n_j\left(f_{1,j} + i\, f_{2,j}\right). \quad (1)$$

Here, r_e is the classical electron radius, λ is the wavelength of the light in vacuum, n_j is the number of atoms of type j per unit volume, and $f_{1,j}$ and $f_{2,j}$ are the real and imaginary parts of the unitless atomic scattering factor for that type of atom. The scattering factors are tabulated in multiple databases including the Center for X-ray Optics (CXRO), which is the one we use in this experiment [7].

Figure 2. Intensity reflectometry on a 100 nm Au thin film on Si substrate. The measured reflectivity (black datapoints) and the theoretical solution fit (solid light green). Additional theoretical curves calculated from the found solution with varied surface roughness are also shown in dotted lines. Inset: cross-sectional sample schematic and solved parameters (surface roughness and density of the Au layer). Figure adapted from [3].
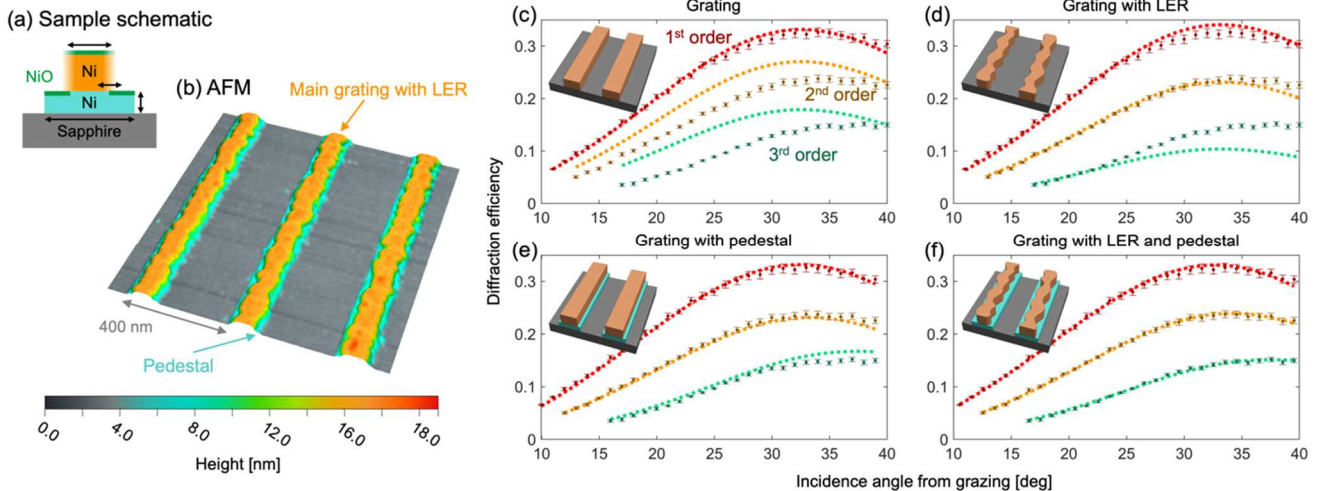
Then, the index of refraction is used in Parratt formalism calculations to predict the complex reflectivity from a transversely uniform region or a large structure (i.e., with a width many times the wavelength). This formalism calculates both the amplitude and the phase of the reflected (or transmitted) wave as it irradiates a multilayered stack at a given incidence angle and wavelength. Additionally, Parratt formalism permits the use of Névot-Croce factors to approximate the effect of surface and interface roughness on reflectivity [8-10].

Figure 2 shows the measured reflectivity from a gold thin film sample as a function of the incidence angle. One thing to note is that the use of the beam splitter effectively account for incident beam power fluctuation, giving error bars of ~0.1%. In this use case, the model of the Au thin film is parametrized by the surface roughness and the mass density of the gold.

A multi-variable optimization scheme is then used to fit our model to the measured data. While many such algorithms exist, we use the genetic algorithm, which is an optimization method that is based on natural selection, with MATLAB's *ga()* function. The genetic algorithm has been shown to work well with X-ray Reflectivity (XRR) measurements due to its robustness and ability to find the global minimum when many local minima are present in the error landscape. Additionally, we can run the algorithm multiple times with different sets of initial populations to verify that the found solution is indeed the global minimum [11,12].

After running the genetic algorithm and verifying the results, we report that the fitted model parameters are $1.5 \, nm$ for the Au surface roughness and $18.5 \, g/cm^3$ for the Au mass density. Moreover, the parametrized model demonstrates great sensitivity ($< 1 \, nm$) in the surface roughness, as shown in different colored curves in Figure 2.

4. SCATTEROMETRY

The second mode is scatterometry, where we measure the diffraction efficiencies at some or many diffracted orders as functions of the incidence angle, using just one wavelength.

The physical forward model for this mode entails not only the IMD calculator but also the Fourier Optics component that takes into the account the transverse geometry of the sample as well as the propagation [13].

As a demonstration, we measured Ni line gratings with a nominal 100 nm linewidth, 400 nm period, and 12.9 nm height patterned using electron lithography on a polished sapphire substrate. As shown by Figure 3, detailed material parameters such as line edge roughness as well as some unexpected features were extracted by solving for the inverse problem related to the diffraction efficiencies. Using the same optimization routine, we are able to extract the width and line edge roughness of the main grating, and the width and height of the pedestal. Furthermore, we can achieve sub-nanometer confidence intervals for the grating width, line edge roughness, and the pedestal height.

The forward model mentioned above only works for sufficiently thin sample, with nanostructures that are short compared to the wavelength of the light. When the structures of a sample become comparably tall relative to the wavelength of illumination, the propagation models of Fourier optics are no longer accurate as they do not account for the explicit 3D nature of the sample. Therefore, for such samples, a more accurate electromagnetic solver must be used to model the observed diffraction patterns. Rigorous Coupled Wave Analysis (RCWA) is used for the characterization of polymer-based optical metasurface samples we received from a collaborator [14,15]. These samples feature hole structures that have high aspect ratio. The depths of these holes reach many times the wavelength of our illumination. Preliminary fits to the diffracted first-order efficiency as well as the models of the two different hole structures are shown in Figure 4.
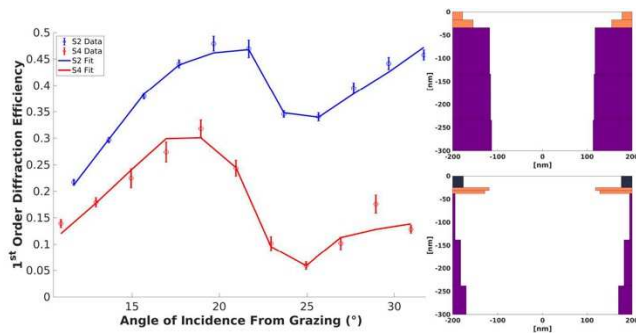

Figure 3. Scatter-reflectometry on Ni line gratings on a sapphire substrate. (a) Cross-sectional sample schematic and solved parameters. (b) Atomic force microscopy image of the sample. (c–f) 1st, 2nd, and 3rd order EUV diffraction efficiency as a function of the incidence angle, and best fits obtained for: (b) simple rectangular grating; (c) grating with line edge roughness (LER); (d) grating with pedestal; and (e) grating with LER and pedestal. Figure adapted from [3].

Figure 4. Polymer Metamaterial Fits and Models. (Left) First order diffraction efficiency. Data and RCWA model fits for samples S2 and S4. (Right Top) S2 model cross-sectional visualization showing the computational layers and color-coded layer compositions. (Right bottom) S4 model cross-sectional visualization showing the computational layers and color-coded layer compositions.

5. COHERENT DIFFRACTIVE IMAGING REFLECTOMETRY

The third mode is coherent diffractive imaging reflectometry, where quantitative imaging of the sample's complex reflectivity (both amplitude and phase shifts upon reflection) is achieved through ptychography, and subsequent device parameters were extracted using reflectometry.

Ptychography solves the phase retrieval inverse problem by collecting far-field intensity of the diffraction patterns through raster scanning and solving for the missing phase information through an iterative algorithm [16-19]. As ptychography extracts the complex-valued reflectance of the sample, we can repeat this process at multiple angles of incidence. In particular, the phase of the light upon reflection exhibits high sensitivity to the elemental composition and surface topography. Therefore, by combining ptychography with reflectometry, we can perform reflectometry in a spatially resolved manner, i.e., imaging reflectometry [4].

We demonstrated imaging reflectometry on a calibrated AFM test sample from BudgetSensors (CS-20NG-UM) that contains SiO_2 structures on Si substrate. Solving the inverse problem of phase retrieval, we were able to extract both the amplitude and phase information of the sample with good spatial resolution within a field of view of about 10 um. From the phase shift images, we can select representative areas of the structured and substrate regions to measure the angle-dependent phase shifts across the two types of sample regions. Using our Parratt formalism calculator, a model of each sample region is constructed with parameterized SiO2 structure height and the (passive) SiO2 top layer thickness on the substrate. The model is then wrapped within a genetic algorithm optimization to fit the predicted and measured phase shifts with respect to sample parameters. The sample schematic, CDI reconstructions at each angle measured, and fit phase shift measurement is shown in Fig. 5. The measured SiO2 thickness was 3.0 nm and the measured structure height was 20.1 nm. Both measurements are determined with sub-

nm confidence intervals and are in good agreement with manufacturer provided specifications (2.5 and 20.8+-0.4 nm respectively).
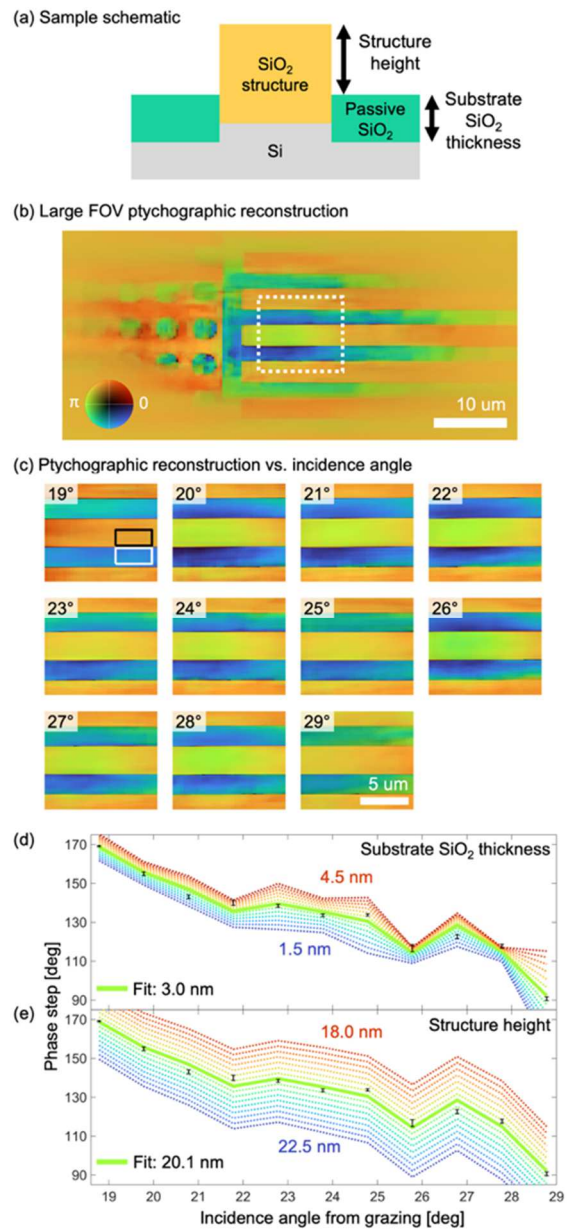
Figure 5. Imaging reflectometry on SiO₂ structures on a Si substrate. (a) Sample schematic and the two measured parameters. (b) Ptychographic reconstruction of the sample at 24 degrees from grazing. The brightness corresponds to the amplitude and the hue to the phase, as indicated by the color wheel, which is shared with (c). The white dotted rectangle indicates the cropped region for (c) and corresponds roughly to the area covered by the $1/e^2$ extent of the probe. (c) Center area of the ptychographic reconstructions taken at 11 incidence angles. Black and white rectangles shown in the 19-degree reconstruction indicate the pixels used in regions on the structure and the substrate respectively to calculate the phase-step curve. (d–e) The measured phase step between the structure and the substrate (black datapoints), and the theoretical solution fit (solid light green). Also shown are the theoretical curves calculated from the found solution with varied substrate SiO₂ thickness between 1.5 and 4.5 nm in 0.25 nm increment in (d), and varied structure height between 18.0 and 22.5 nm in 0.3 nm increment in (e). Figure adapted from [3].

6. References

[1] G. Orji, B. Bunday, and Y. Obeng, International Roadmap for Devices and Systems: Metrology (IEEE, 2022).

[2] N. G. Orji et al., "Metrology for the next generation of semiconductor devices," *Nat Electron*, vol. 1, no. 10, pp. 532–547, Oct. 2018, doi: 10.1038/s41928-018-0150-9.

[3] Y. Esashi et al., "Tabletop extreme ultraviolet reflectometer for quantitative nanoscale reflectometry, scatterometry, and imaging," *Review of Scientific Instruments*, vol. 94, no. 12, p. 123705, Dec. 2023, doi: 10.1063/5.0175860.

[4] M. Tanksalvala et al., "Nondestructive, high-resolution, chemically specific 3D nanostructure characterization using phase-sensitive EUV imaging reflectometry," *Sci. Adv.*, vol. 7, no. 5, p. eabd9667, Jan. 2021, doi: 10.1126/sciadv.abd9667.

[5] N. J. Brooks et al., "Temporal and spectral multiplexing for EUV multibeam ptychography with a high harmonic light source," *Opt. Express*, vol. 30, no. 17, p. 30331, Aug. 2022, doi: 10.1364/OE.458955.

[6] D. T. Attwood and A. Sakdinawat, *X-rays and extreme ultraviolet radiation: principles and applications*, 2nd ed. Cambridge: Cambridge university press, 2016.

[7] B. L. Henke, E. M. Gullikson, and J. C. Davis, "X-Ray Interactions: Photoabsorption, Scattering, Transmission, and Reflection at E = 50-30,000 eV, Z = 1-92," *Atomic Data and Nuclear Data Tables*, vol. 54, no. 2, pp. 181–342, Jul. 1993, doi: 10.1006/adnd.1993.1013.

[8] L. G. Parratt, "Surface Studies of Solids by Total Reflection of X-Rays," *Phys. Rev.*, vol. 95, no. 2, pp. 359–369, Jul. 1954, doi: 10.1103/PhysRev.95.359.

[9] L. Névot and P. Croce, "Caractérisation des surfaces par réflexion rasante de rayons X. Application à l'étude du polissage de quelques verres silicates," *Rev. Phys. Appl. (Paris)*, vol. 15, no. 3, pp. 761–779, 1980, doi: 10.1051/rphysap:01980001503076100.

[10] Y. Esashi, M. Tanksalvala, Z. Zhang, N. W. Jenkins, H. C. Kapteyn, and M. M. Murnane, "Influence of surface and interface roughness on X-ray and extreme ultraviolet reflectance: A comparative numerical study," *OSA Continuum*, vol. 4, no. 5, p. 1497, May 2021, doi: 10.1364/OSAC.422924.

[11] A. D. Dane, A. Veldhuis, D. K. G. de Boer, A. J. G. Leenaers, and L. M. C. Buydens, "Application of genetic algorithms for characterization of thin layered materials by glancing incidence X-ray reflectometry," *Physica B: Condensed Matter*, vol. 253, no. 3–4, pp. 254–268, Oct. 1998, doi: 10.1016/S0921-4526(98)00398-6.

[12] A. Ulyanenkov, K. Omote, and J. Harada, "The genetic algorithm: refinement of X-ray reflectivity data from multilayers and thin films," *Physica B: Condensed Matter*, vol. 283, no. 1–3, pp. 237–241, Jun. 2000, doi: 10.1016/S0921-4526(99)01972-9.

[13] J. W. Goodman, *Introduction to Fourier optics*, Third edition. Englewood, Colorado: Roberts & Company, 2005.

[14] M. G. Moharam, T. K. Gaylord, E. B. Grann, and D. A. Pommet, "Formulation for stable and efficient implementation of the rigorous coupled-wave analysis of binary gratings," *J. Opt. Soc. Am. A*, vol. 12, no. 5, p. 1068, May 1995, doi: 10.1364/JOSAA.12.001068.

[15] M. G. Moharam and T. K. Gaylord, "Rigorous coupled-wave analysis of planar-grating diffraction," *J. Opt. Soc. Am.*, vol. 71, no. 7, p. 811, Jul. 1981, doi: 10.1364/JOSA.71.000811.

[16] D. Sayre, "Some implications of a theorem due to Shannon," *Acta Cryst*, vol. 5, no. 6, pp. 843–843, Nov. 1952, doi: 10.1107/S0365110X52002276.

[17] J. M. Rodenburg and H. M. L. Faulkner, "A phase retrieval algorithm for shifting illumination," *Applied Physics Letters*, vol. 85, no. 20, pp. 4795–4797, Nov. 2004, doi: 10.1063/1.1823034.

[18] A. M. Maiden and J. M. Rodenburg, "An improved ptychographical phase retrieval algorithm for diffractive imaging," *Ultramicroscopy*, vol. 109, no. 10, pp. 1256–1262, Sep. 2009, doi: 10.1016/j.ultramic.2009.05.012.

[19] P. Thibault, M. Dierolf, O. Bunk, A. Menzel, and F. Pfeiffer, "Probe retrieval in ptychographic coherent diffractive imaging," *Ultramicroscopy*, vol. 109, no. 4, pp. 338–343, Mar. 2009, doi: 10.1016/j.ultramic.2008.12.011.